Conformal Piezoelectric Energy Harvesting and Storage From Motions of the Heart, Lung and Diaphragm

Canan Dagdeviren[a,1], Byung Duk Yang[a,1], Yewang Su[b,c,1], Phat Le Tran[d], Pauline Joe[a], Eric Anderson[a], Jing Xia[b,c], Vijay Doraiswamy[d], Behrooz Dehdashti[e], Xue Feng[f], Bingwei Lu[b], Robert Poston[e], Zain Khalpey[e], Roozbeh Ghaffari[g], Yonggang Huang[c], Marvin J. Slepian[d,h], John A. Rogers[a,i,2]

[a]*Department of Materials Science and Engineering, Beckman Institute for Advanced Science and Technology, and Frederick Seitz Materials Research Laboratory, University of Illinois at Urbana-Champaign, Urbana, IL 61801*
[b]*Center for Mechanics and Materials, Tsinghua University, Beijing 100084, China*
[c]*Department of Civil and Environmental Engineering, Department of Mechanical Engineering, Center for Engineering and Health and Skin Disease Research Center, Northwestern University, Evanston, IL 60208*
[d]*Department of Medicine & Sarver Heart Center, The University of Arizona, Tucson, AZ 85724*
[e]*Department of Surgery, The University of Arizona, Tucson, AZ 85724*
[f]*Department of Engineering Mechanics, Tsinghua University, Beijing 100084, China*
[g]*MC10 Inc., Cambridge, MA 02140*
[h]*Department of BioMedical Engineering, The University of Arizona, Tucson, AZ 85724*
[i]*Department of Chemistry, Department of Mechanical Science and Engineering and Department of Electrical and Computer Engineering, University of Illinois at Urbana-Champaign, Urbana, IL 61801*

[1]C.D., B. D.Y., and Y.S. contributed equally to this work.
[2]To whom correspondence should be addressed. E-mail: jrogers@illinois.edu

Supporting Information

1. SI Materials and Methods

1.1. Fabrication of Lead Zirconate Titanate (PZT) Ribbons Array and Transferprinting Them on PI

PZT ribbons embedded in capacitor type structures with top and bottom electrodes were fabricated as following. The top electrode was formed by deposition of Au/Cr (200 nm/10 nm) with an electron beam evaporator on the surface of a multilayer stack of $Pb(Zr_{0.52}Ti_{0.48})O_3/Pt/Ti/SiO_2$ (500 nm/300 nm/20 nm/600 nm; INOSTEK) on a silicon wafer. Coating the wafer with photoresist (PR, AZ5214E) followed by patterning by photolithography defines the top electrode areas (50 µm x 2 mm) for each PZT ribbon. Au and Cr layers were etched with gold etchant (TFA, Transene Company Inc., USA) and CR-7 chrome etchant (OM Group, USA), respectively. PZT ribbons with thickness of 500 nm and an area of 100 µm x 2.02 mm were created by wet chemical etching with HNO_3 (nitric acid): BHF (buffered hydrogen fluoride): H_2O (DI water) = 4.51:4.55:90.95 through a hard-baked mask of PR (AZ4620, Clariant) (See Fig. S1*A*). The hard baking involved 80 °C for 5 minutes, 110 °C for 30 minutes and then 80°C for 5 minutes (See Fig. S1*B*). The bottom Pt/Ti electrode with area of 140 µm x 2.02 mm was patterned by wet chemical etching with HCl (hydrochloric acid) : HNO_3 : DI water = 3:1:4 at 95°C through a hard baked mask of AZ4620. The PZT layers were protected by photolithographically patterned PR during partially removal of the sacrificial layer, SiO_2 with dilute HF (hydrofluoric acid) (DI water: 49% HF = 1:3). Hard baked photoresist mask was completely removed in an acetone bath for 3 hours after etching the SiO_2.

A PDMS stamp for transfer was fabricated by casting a mixture of PDMS (Sylgard 184, Dow Corning; 10:1 ratio of prepolymer to curing agent) in a plastic petri dish, and curing at

room temperature for 24 hours. Next, the stamp was conformally contacted on the top of the ribbons (See Fig. S1*C*). The devices were retrieved by peeling the stamp away from the Si wafer and then transfer printed on a film of PI (75 μm, DuPont, USA). This film was formed by spin-coating a layer of poly(pyromellitic dianhydride-co-4,4'-oxydianiline) amic acid solution, to a thickness of 1.2 μm (See Supplementary Fig. S1*D*). The printed PZT ribbons on the PI were spin-coated with another layer of PI for encapsulation and hard baked at 250 ^{o}C in a vacuum oven.

To open contact holes for the top and bottom electrodes, the device on PI was patterned with photoresist (PR, AZ 4620), and developed with diluted AZ®400K developer (AZ Electronic Materials, USA) (deionized water (DI) : 400 K developer = 1:2). The PI was etched in reactive ion etching (RIE, March) to open contact holes. Connection lines were obtained by the deposition of Au/Cr (200 nm/10 nm) using electron beam evaporation. The interconnection lines were spin-coated with another layer of PI for encapsulation and hard baked at 250 ^{o}C in a vacuum oven.

1.2. Poling of the PZT thin film and device analysis via mechanical testing

The PZT thin films sandwiched between Ti/Pt (20 nm/300 nm) bottom electrode and Cr/Au (10 nm/200 nm) were poled with an electric field of 100 kV/cm at 150°C for 2 hours. A semiconductor parameter analyzer (4155C, Agilent) was used to measure the open voltage and short current values of mechanical energy harvester. Figure S15 shows a mechanical bending stage for testing the PZT MEH. The system includes a high precision linear stage (ATS100-150; Aerotech, Inc.; USA), equipped with precision ground ball screw, noncontact rotary encoder with 1000 line/rev, and brushless servomotor to achieve a motion with an accuracy of ±0.5 μm

and a bidirectional repeatability of ±0.3 µm over 150 mm stage motion range. The stage can achieve velocities up to 100 mm/sec with maximum side load of 100 N in horizontal configuration. The stage motion was controlled with a Soloist single axis PWM digital controller (SOLOISTCP20; Aerotech, Inc.; USA) and USB interface. Additionally, two U-Form Vise grip (TH240k, Grip Engineering Thümler GmbH; Germany) were attached to the stage. Pyramid shape jaws (TH240k-BP, Grip Engineering Thümler GmbH; Germany) were attached to the vices to achieve maximum tensile gripping force of 2.5 kN of the specimen during the test. A LabVIEW (National Instruments Corporation; USA) based program was designed to control the stage to perform the test cycle (Fig. S15).

1.3. *In Vitro* Biocompatibility Assessment of the Flexible PZT MEH

Aortic smooth muscle cells (SMC) were harvested from albino Sprague-Dawley rat (with IACUC approval protocol from the University of Arizona) and subsequently cultured in Dulbecco's Modified Eagle Medium (DMEM) supplemented with 10% (v/v) fetal calf serum, 2% (v/v) of 0.2 M glutamine, 1% (v/v) of antibiotic/antimycotic solution. All cell culture supplements and medium were either purchased at Invitrogen (Grand Island, NY, USA) or BioWhittaker (East Rutherford, NJ, USA). SMCs were then sub-cultivated and cultured in an incubator at 37 ºC, 5% CO_2, and 95% relative humidity to passages 2-5 before subjecting to ribbonping (trypsin-EDTA), cell counting, and seeding on the sterilized fibronectin (BD-Biosciences, San Jose, CA, USA) coated PZT MEH.

To prepare for biocompatibility studies, PZT MEH ribbons were cut into 1 cm^2 coupons to fit in a 24 well culture plate. These coupons were then cleaned using Basic Harrick Plasma (Ithaca, NY, USA) for 10 minutes at 1 torr to increase surface hydrophobicity. Subsequently, coupons were sterilized under UV light for 30 minutes then coated with 150 µL of 1 mg/ml fibronectin

for another 15 minutes. Any excess fibronectin was removed and allowed to dry in the culture hood for another 15 minutes prior to $5x10^4$ SMCs cultivation for 1, 3, and 9 days at 37 ºC, 5% CO_2, and 95% relative humidity. Medium was changed every 24 hours.

At the given latter endpoints, SMCs were stained using actin cytoskeleton/focal adhesion staining kit (Millipore, MA, USA). Cells were fixed with 4% paraformaldehyde for 15 minutes, then washed and permeated the membrane with 0.05% Triton X for 5 minutes. Cells were washed and blocked with 1% protein standard (fractionated bovine serum albumin) in PBS at pH7.4 and subsequently stained with anti-vinculin for 1 hour at room temperature. Cells were washed and stained with fluorescein isothiocyanate conjugated mouse anti-immunoglobulin G (mIgG-FITC) to label vinculin and tetramethyl rhodamine isothicyanate (TRITC) conjugated Phalloidin to selectively label F-actin. After washing off all the excess stains, cells were then mounted in vector shield with DAPI and imaged using the Nikon C1Si Laser Scanning Confocal Fluorescence Microscope. SMCs on the PZT MEH exhibit normal morphology where intact cytoskeletal fibers, nucleus, and focal adhesion points are present, suggesting that the surface of PZT MEH is a suitable environment for cell growth.

Scanning electron microscopy (SEM, FEI Inspec S, Thermo, Rockford, IL, USA) was also utilized to physically demonstrate the adherent of cells on PZT MEH ribbons. Briefly, SMCs after 9 days of culture were fixed in 5% Glutaraldehyde in PBS at pH7.4 (100% fixator) then subjected to a graded series of water and ethanol (100% fixator → 3:1 → 1:1 → 1:3 → 100% Distilled water → 3:1 → 1:1 → 1:3 → 100% Ethanol. Samples were soaked for 5 min at each step. Finally, Samples were freeze-fried using critical point drying (CPD, EMS #3100, Hatfield, PA, USA). A more detailed CPD protocol can be found in (1). Subsequently, samples were sputter-coated with gold at about 5-8 nm thick and imaged at 30 kV with aperture spot size of 3.

To evaluate the biocompatibility of the PZT MEH structures, the viability and cytotoxicity of SMC were determined after 9 days of cultivation by utilizing two color fluorescence LIVE/DEAD viability (Invitrogen) assay and Lactate Dehydrogenase (LDH) assay (Thermo, IL, USA), respectively. For LIVE/DEAD assay, SMCs grown on PZT MEH ribbon after 9 days were prepared and stained according to manufacture protocol with the exception that samples were mounted in Flouroshield containing DAPI (Sigma Aldrich, St. Louis, MO, USA). Briefly, the culture medium was aspirated from each of the wells then rinsed three times with 1x PBS, and a working solution (consisting of 5 mL 1x PBS, 10 µL of 2mM EthD-1, and 2.5 µL of 4mM Calcein AM) was added to cover each of the samples. The submerged samples were incubated for 30 minutes at 37^{O}C. After the incubation period, the working solution was removed, and the samples were rinsed once with 1x PBS, then mounted and immediately imaged with the Nikon C1Si fluorescence microscope. For the LDH cytotoxicity assay, 50 µL medium from cells grown on fiber surfaces at the latter given endpoints (ie. 1, 3, and 9 days) were mixed with 50 µL reaction mixture (prepared according to the manufacture recipe) in a 96 wells plate for 30 minutes at room temperature. Stop solution (50 µL) was added and the plate was read at 490/680nm. Mean percent of healthy cells was reported with standard error of mean. All statistical analysis was performed using Microsoft Excel 2010. TTEST was analyzed using one-tailed distribution and two-sample unequal variance type. Statistical significance of differences between the means was determined using a student's t-test ($p = 0.05$).

1.4. Implantation of the PZT MEH: an *In vivo* Study

All animals received humane care and were handled in accordance with IACUC approval protocol at the University of Arizona Animal Care Center. Male Corriente bovine (n=4, 90-140

kg) and domestic ovine (n=1, 45 kg) were used. Animals fasted for 12 hours without food and 8 hours without water prior to left thoracotomy. Animals were operated off-pump, without cardiopulmonary bypass and survived for two hours post-surgery.

Briefly, animal were restrained with Telazol (2.2 mg/kg Intramuscular (IM) or 4 mg/kg Intravenous (IV)), weighed, and anesthetized with 3-5% Isoflurane induction administered via the facemask. An oral endotracheal tube was then placed. Butorphanol (0.01-0.02 mg/kg) and Xylazine (0.1-0.2 mg/kg) were administered via intramuscular (IM) injection into the hamstring muscle to relieve pain. Animal were clipped, shaved, and prepped for the surgery. Glycopyrrolate was administered at 0.002-0.005 mg/kg Intravenous (IV) when bradycardia is present. Animal was then intubated and anesthesia was further maintained at 0.5-3% Isoflurane and at room temperature throughout the study. An orogastric tube was placed to decompress the rumen. A triple lumen catheter (7-8F) was inserted percutaneously into the right jugular vein for IV line for drip infusion of lactated ringers to maintain hydration and for delivery of drugs. An arterial pressure catheter was placed in the carotid artery and ECG was connected to monitor the animal.

Prior to surgery, Ketamine (3-4 mg/kg) and Midazolem (0.25 mg/kg) were inducted intravenously to relax muscle. Pancuronium Bromide (0.04-0.1 mg/kg, IV) were used to block myoneural junctions. Fentanyl (loading dose of 5 µg/kg and dripping dose of 5 to 10 µg/kg/hr), Lidocaine (loading dose of 2 mg/kg and dripping dose of 2 mg/kg/hr), and Ketamine (loading dose of 2 mg/kg and dripping dose of 2 mg/kg/hr) were infused intravenously in addition to inhalant throughout the operation. Left thoracotomy was performed and cauterized with the electrosurgico knife (Conmed Excalibur Plus, Utica, NY, USA). The fifth left rib was snipped and a retractor was used to expose solid tissues like the heart, lung, and diaphragm. Amiodarone

(loading dose of 50 mg IV bolus and dripping dose of 0.3 to 0.9 mg/kg/hr) was administered to control arrhythmias prior to the manipulation of the heart. PZT MEH was then sutured to solid tissues using 2-0 bladed polypropylene (Ethicon, San Angelo, TX, USA). A cable (ACF; Anisotropic conductive film, 3M Co.) was connected to a voltmeter storage monitor systems. To evaluate the responsiveness of the PZT MEH, temporary pacemaker (Medtronic 5388, Minneapolis, MN, USA) and Dobutamine (5-15 $\mu g \cdot kg^{-1} \cdot min^{-1}$, IV) was used to fluctuate the heart rate. After all initial readings, animal were survived for 2 hours to allow the PZT MEH to recharge the battery. Incision sites were closed using the standard technique. At the termination of the surgery, animal were humanely euthanized with 30 ml of Beuthanasia while still under general anesthesia. The PZT MEH was then removed for detailed examination and reading.

2. Theory

2.1. Mechanics analysis

For the out-of-plane displacement $w = A\left[1+\cos\left(2\pi x_1/L\right)\right]/2$ shown in Fig. S6*A* for plane-strain analysis ($\varepsilon_{22}=0$), the bending energy in PI is related to the curvature w'' by $\left(\overline{EI}_{PI}/2\right)\int(w'')^2\,ds$, where the integration is over the PI length, and $\overline{EI}_{PI}=\left(\bar{E}_{PI}t_{PI}^3\right)/12$, $\bar{E}_{PI}$ and t_{PI} are the plane-strain bending stiffness, plane-strain modulus, and thickness of PI, respectively. The membrane energy can be obtained following the same approach of Song et al. (2). Minimization of the total energy (sum of bending and membrane energies) gives the amplitude *A* as

$$A=\frac{2}{\pi}\sqrt{L\cdot\Delta L-\frac{\pi^2 t_{kapton}^2}{3}}\approx\frac{2}{\pi}\sqrt{L\cdot\Delta L}\,, \tag{S1}$$

where the last approximation holds when the compression of PI ΔL is much larger than its critical value $\pi^2 t_{PI}^2/(3L)$ to initiate buckling. For a 75 μm-thick and 2.5 cm-long PI, $\pi^2 t_{PI}^2/(3L)$ ~0.74 μm is negligible as compared to compression $\Delta L = 1.5 \sim 10$ mm in the experiments.

The bending moment *M* in PI is related to the curvature w'' by $M = \overline{EI}_{PI} w''$. For the part of PI covered by the PZT ribbons (Fig. S6*B*), the local curvature is reduced to $M/\overline{EI}_{comp}$ due to the additional bending stiffness of PZT ribbons, where $\overline{EI}_{comp} = \sum_{i=1}^{n} \bar{E}_i t_i \left[t_i^2/3 + \left(\sum_{j=1}^{i} t_j - y_{neutral} \right) \left(\sum_{j=1}^{i} t_j - y_{neutral} - t_i \right) \right]$ is the effective bending stiffness of multi-layer structure (Fig. S6B) with PI as the 1st layer (*i*=1) and the summation over all *n* layers, $\bar{E}_i$ and t_i are the plane-strain modulus and thickness of the ith layer, respectively, and $y_{neutral} = \left[\sum_{i=1}^{n} \bar{E}_i t_i \left(2\sum_{j=1}^{i} t_j - t_i \right) \right] \Big/ \left(2\sum_{i=1}^{n} \bar{E}_i t_i \right)$ is the distance from the neutral mechanical plane to the bottom of 1st (PI) layer. The membrane strain in PZT is the axial strain at the center of PZT ribbons, and is given by

$$\varepsilon_m = \left(\overline{EI}_{PI} / \overline{EI}_{comp} \right) w'' h , \tag{S2}$$

where *h* is the distance from the center of each PZT ribbon to the neutral mechanical plane of the cross section as shown in Fig. S6*B*. For the length of PZT ribbons much smaller than that of the PI, w'' is evaluated at the center x_1=0 of PZT ribbons as $w'' = -4\pi\sqrt{\Delta L/L}/L$, which gives the membrane strain as shown in Eq. (1) in the main text. For the structure shown in Fig. S6*B*, $\bar{E}_1 = 2.83\,GPa$ and $t_1 = 75\,\mu m$ for PI, $\bar{E}_2 = 2.83\,GPa$ and $t_2 = 1.2\,\mu m$ for the PI layer, $\bar{E}_3 = 129\,GPa$ and $t_3 = 20\,nm$ for the Ti layer, $\bar{E}_4 = 196\,GPa$ and $t_4 = 0.3\,\mu m$ for the Pt layer,

$\bar{E}_5 = 69.2\,GPa$ and $t_5 = 0.5\,\mu m$ for the PZT layer, $\bar{E}_6 = 292\,GPa$ and $t_6 = 10\,nm$ for the Cr layer, $\bar{E}_7 = 96.7\,MPa$ and $t_7 = 0.2\,\mu m$ for the Au layer, and $\bar{E}_8 = 2.83\,GPa$ and $t_8 = 1.2\,\mu m$ for the PI layer; these give $\overline{EI}_{PI}/\overline{EI}_{comp}$ =0.45, $y_{neutral}$=52.0 μm and $h = (t_1 + t_2 + t_3 + t_4 + t_5/2) - y_{neutral}$ =24.7 μm.

2.2. Piezoelectric analysis

The constitutive model of piezoelectric materials gives the relations among the stress σ_{ij}, strain ε_{ij}, electrical field E_i and electrical displacement D_i as

$$\begin{Bmatrix} \sigma_{11} \\ \sigma_{22} \\ \sigma_{33} \\ \sigma_{23} \\ \sigma_{31} \\ \sigma_{12} \end{Bmatrix} = \begin{bmatrix} c_{11} & c_{12} & c_{13} & 0 & 0 & 0 \\ c_{12} & c_{11} & c_{13} & 0 & 0 & 0 \\ c_{13} & c_{13} & c_{33} & 0 & 0 & 0 \\ 0 & 0 & 0 & c_{44} & 0 & 0 \\ 0 & 0 & 0 & 0 & c_{44} & 0 \\ 0 & 0 & 0 & 0 & 0 & (c_{11} - c_{12})/2 \end{bmatrix} \begin{Bmatrix} \varepsilon_{11} \\ \varepsilon_{22} \\ \varepsilon_{33} \\ 2\varepsilon_{23} \\ 2\varepsilon_{31} \\ 2\varepsilon_{12} \end{Bmatrix} - \begin{bmatrix} 0 & 0 & e_{31} \\ 0 & 0 & e_{31} \\ 0 & 0 & e_{33} \\ 0 & e_{15} & 0 \\ e_{15} & 0 & 0 \\ 0 & 0 & 0 \end{bmatrix} \begin{Bmatrix} E_1 \\ E_2 \\ E_3 \end{Bmatrix}, \quad \text{(S3)}$$

$$\begin{Bmatrix} D_1 \\ D_2 \\ D_3 \end{Bmatrix} = \begin{bmatrix} 0 & 0 & 0 & 0 & e_{15} & 0 \\ 0 & 0 & 0 & e_{15} & 0 & 0 \\ e_{31} & e_{31} & e_{33} & 0 & 0 & 0 \end{bmatrix} \begin{Bmatrix} \varepsilon_{11} \\ \varepsilon_{22} \\ \varepsilon_{33} \\ 2\varepsilon_{23} \\ 2\varepsilon_{31} \\ 2\varepsilon_{12} \end{Bmatrix} + \begin{bmatrix} k_{11} & 0 & 0 \\ 0 & k_{22} & 0 \\ 0 & 0 & k_{33} \end{bmatrix} \begin{Bmatrix} E_1 \\ E_2 \\ E_3 \end{Bmatrix}. \quad \text{(S4)}$$

The plane-strain condition $\varepsilon_{22} = 0$ of PZT ribbons, together with $\sigma_{33} = 0$ from the traction free on the top surface of the structure, gives $D_3 = \bar{e}\varepsilon_{11} + \bar{k}E_3$, where $\bar{e} = e_{31} - (c_{13}/c_{33})e_{33}$ and $\bar{k} = k_{33} + (e_{33}^2/c_{33})$ are the effective piezoelectric constants. The electrical displacement can be further obtained as

$$D_3 = \bar{e}\varepsilon_m + \frac{\bar{k}V}{Nt_{PZT}} \tag{S5}$$

from the charge equation $dD_3/dx_3 = 0$ and the relation $E_3 = -\partial\phi/\partial x_3$ between the electrical field and electrical potential, together with the boundary condition that the voltage difference between the bottom and top of PZT is V/N, where V is total voltage between the two ends of the N groups of PZT ribbons in series, and t_{PZT} is the thickness of PZT ribbons. Eq. (S5) shows that the electrical displacement is linear with the membrane strain of PZT ribbons, and is independent of the bending strain. Therefore the bending strain does not contribute to the voltage and current output of the MEH given in the following.

2.3. Current

The voltage V across the two ends of the N groups of PZT ribbons in series is zero after the PZT ribbons are connected to an ampere meter (Fig. S6*C*). The electrical displacement in Eq. (S5) then becomes $D_3 = \bar{e}\varepsilon_m$, where ε_m is given in Eq. (1) in the main text. Its rate gives the current $I = -A_{PZT}\dot{D}_3$, or equivalently Eq. (2) in the main text, where $A_{PZT} = m\left(w_{PZT,1}l_{PZT,1} + w_{PZT,2}l_{PZT,2}\right)$ is total area of PZT ribbons in each group; $m = 10$ is the number of PZT ribbons in each group, $w_{PZT,1} = 100\,\mu\text{m}$, $w_{PZT,2} = 140\,\mu\text{m}$, $l_{PZT,1} = 2\,\text{mm}$ and $l_{PZT,2} = 160\,\mu\text{m}$ are the widths and lengths of the two rectangular parts of each PZT ribbon, respectively (Fig. S6*B*).

2.4. Voltage

For voltage measurement, the voltage V in Eq. (S5) across the two ends of the *N* groups of PZT ribbons in series is no longer zero after the PZT ribbons are connected to a voltmeter (Fig. S6*C*). The rate of the displacement in Eq. (S5) gives the current $I = -A_{PZT}\left\{\bar{e}\dot{\varepsilon}_m + \left[\bar{k}/\left(Nt_3\right)\right]\dot{V}\right\}$, which, together with the Ohm's law gives Eq. (4) in the main text.

2.5. Rectifier

For current measurements with the rectifier (Fig. S6*D*), the resistance across the PZT groups is no longer zero because of the resistance of the rectifier $R_{rectifier}$. Instead it is the same as the voltage measurement shown Fig. S6*C* except that the resistance of the voltmeter R is replaced by $R_{rectifier}$. After this replacement Eq. (5) still holds, but is taken by its absolute value because of the rectifier (3). The current is then obtained from Ohm's law as

$$I = \frac{1}{R_{rectifier}} \frac{\left(-\bar{e}\right) Nt_{PZT}}{\bar{k}} e^{-\frac{Nt_{PZT}}{A_{PZT} R_{rectifier} \bar{k}} t} \left| \int_0^t \frac{d\varepsilon_m}{dt} e^{\frac{Nt_{PZT}}{A_{PZT} R_{rectifier} \bar{k}} t} dt \right|. \tag{S6}$$

For the voltage measurement with the rectifier (Fig. S6*D*), the resistance R is replaced by $R + R_{rectifier}$. After this replacement Eq. (5) still holds for the voltmeter and rectifier in series, and the voltage on the voltmeter is then obtained by multiplying the factor $R/\left(R + R_{rectifier}\right)$ of the absolute value of Eq. (5) as

$$V = \frac{R}{R + R_{rectifier}} \frac{\left(-\bar{e}\right) Nt_{PZT}}{\bar{k}} e^{-\frac{Nt_{PZT}}{A_{PZT}\left(R + R_{rectifier}\right) \bar{k}} t} \left| \int_0^t \frac{d\varepsilon_m}{dt} e^{\frac{Nt_{PZT}}{A_{PZT}\left(R + R_{rectifier}\right) \bar{k}} t} dt \right|. \tag{S7}$$

2.6. Direction of bending

Figs. S3 and S4 show the strain in PZT bent along x_1 and x_2 directions, respectively, for the axial compression of $\Delta L = 1.5$, 3, 5 and 10 mm. For the same axial compression ΔL, the strain in PZT bent along x_1 direction is larger than that along x_2 direction, and is therefore more effective for energy harvesting.

2.7. The time-averaged power density

The electrical energy output is obtained by integrating the ratio of the square of the voltage V and the resistance R over total time t_{total} as $W = \int_0^{t_{total}} V^2/R\,dt$ (4). The time-averaged power density is given by $P = W/(t_{total} N A_{PZT})$.

2.8. FEA for the deformation of the stacks

Finite element analysis (FEA) is used to study the deformation of a single PZT MEH and the stacks of 3 and 5 PZT MEHs with spin-casted silicone layer of 10 μm thickness in between. The solid elements in the ABAQUS finite element program (5) are used to mesh all materials, including the PZT ribbons. Fig. S18 shows that the amplitudes of the PZT MEHs in the stacks are very close to that of the single PZT MEH, with the difference less than 1%, which clearly suggests that the soft silicone layers do not make significant contribution to the deformation of the PZT MEHs.

References

1. Thomasson SA, Thomasson JR (2011) A comparison of CPD (critical point drying) and HMDS (hexamethyldisilazane) in the preparation of *Corallorhiza* spp. rhizomes and associated mycorrhizae for SEM (scanning electron microscopy). *Transactions of the Kansas Academy of Science* 114(1&2):129-134.
2. Song J, et al. (2009) Mechanics of noncoplanar mesh design for stretchable electronics circuits. *Journal of Applied Physics* 105(12):123516.
3. Bishop O (2011) *Electronics A First Course*. Elsevier Ltd., Burlington, MA.
4. Andosca R, et al. (2012) Experimental and theoretical studies on MEMS piezoelectric vibrational energy harvester with mass loading. *Sensors and Actuators A* 178:76-87.
5. Dassault Systèmes (2010) Abaqus analysis user's manual v.6.10. Dassault Systèmes Simulia Corp., Providence, RI.

SI Figure Legends

Figure S1. Schematic illustration of procedures for fabricating a PZT MEH on a polyimide (PI) substrate. Schematic illustration of (*A*) array of ribbons of PZT in a capacitor structure on a SiO_2/Si wafer (left). A cross section of one element in this array appears on the right. (*B*) Pattern of photoresist on the array (left), and cross section of one element during undercut etching with dilute HF solution (right). (*C*) Retrieving the array with a PDMS stamp to leave them adhered to the surface of the stamp. (*D*) Result after transfer printing onto a flexible film of PI.

Figure S2. Fabrication steps to fabricate PZT ribbons. Optical microscope image of printed ribbons of PZT on a film of PI (*A*) before bending, (*B*) after bending with the radius of 20 mm curvature and (*C*) with the view of top and bottom connection pads. (*D*) The cross sectional illustration of a ribbon of PZT with top and bottom electrodes, on a PI substrate with a thin overcoat of PI for encapsulation. (*E*) Schematic illustration of PZT ribbons grouped and connected in series.

Figure S3. Results of FEM analysis for strain mapping of the bare PZT ribbons array. (*A*) Deformation of a PZT MEH and (*B*) corresponding strain distributions in the ribbons of PZT. The displacement loads (ΔL) correspond to 0, 1.5, 3, 5 and 10 mm along the x_1 direction, from left to right.

Figure S4. Results of FEM analysis for strain mapping of the bare PZT ribbons array. (*A*) Deformation of a PZT MEH and (*B*) corresponding strain distributions in the ribbons of PZT. The displacement loads (ΔL) correspond to 0, 1.5, 3, 5 and 10 mm along the x_2 direction, from top to bottom.

Figure S5. Experimental and theoretical results for displacement, voltage, and current as a function of time for cyclic bending of a PZT MEH with rectification.

Figure S6. Device layouts and information related to variable names and physical parameters used in calculations. Schematic illustration of (*A*) the theoretical shape for buckling of a PZT MEH under compression, (*B*) top view of a single PZT ribbon capacitor structure (top), and cross section showing

position of the neutral mechanical plane of the device (bottom). A buckled array of PZT ribbon capacitor structures on a PI substrate without (*C*) and with (*D*) rectification.

Figure S7. Images that show the ability of flexible PZT MEHs to conform to various surfaces. Photograph of a PZT MEH (*A*) on a balloon. (*B*) A magnified view of the device. Photograph of a PZT MEH wrapped onto the (*C*) arm and (*D*) finger.

Figure S8. Responses of a PZT MEH for forward and reverse connections. (*A*) Forward and (*B*) reverse connections to the measurement system. (*C*) Open-circuit voltage and (*D*) short-circuit current of a PZT MEH under cyclic bending for these two configurations.

Figure S9. Studies of cycle life in a PZT MEH. Photographs of device clamped in a bending stage with a layer of a transparent gelatine (Knox) on top, in (*A*) flat and (*B*) bent states. Output voltage as a function of time after a single cycle of bending (*C*) and twenty million cycles of bending (*D*).

Figure S10. Output from a PZT MEH mounted on the bovine heart, for different pacing conditions. Voltage as a function of time measured from a PZT MEH on the (*A*) RV, (*B*) LV, and (*C*) free wall of a bovine heart at 0^{O} with respect to the apex, at heart rates of 80, 90, 100, 110, and 120 beats/min.

Figure S11. Output from a PZT MEH mounted on the ovine heart, for different pacing conditions. Voltage as a function of time measured from a PZT MEH on the (*A*) RV, (*B*) LV, and (*C*) free wall of a bovine heart at 0^{O} with respect to the apex, at heart rates of 110, 120 and 130 beats/min; respectively.

Figure S12. Output from a PZT MEH mounted on the bovine heart for different levels of dobutamine infusion. Voltage as a function of time measured from a PZT MEH on the (*A*) LV, (*B*) RV of a bovine heart at 0^{O} with respect to the apex with 0, 2, 5, 10 and 15 $\mu g \cdot kg^{-1} \cdot min^{-1}$ of dobutamine.

Figure S13. Performance of a PZT MEH evaluated with the chest open and closed on a pig model. Photograph of a PZT MEH without battery and rectifier connection on pig heart when the chest is (*A*) open and (*B*) closed. Voltage as a function of time for a PZT MEH on the pig LV with the chest open (*C*) and closed (*D*).

Figure S14. Effect of orientation of the PZT MEH with respect to the apex of a bovine heart. Voltage as a function of time measured on the RV of a bovine heart with 80 beats/min (*A*) at 0^{O} and (*B*) at 45^{O}.

Figure S15. Image of the experimental setup used for bending and cycling tests. (A) The picture here shows testing of a five layer stack of PZT MEHs, with a LabVIEW control interface. A cross sectional image of the stacked device appears in the top left. (B) A photograph of LabVIEW controllable mechanical bending stage.

Figure S16. Output voltage as a function of time measured from a stacked arrangement of PZT MEHs. Experimental and theoretical results for displacement, voltage as a function of time, for four different bending load displacements. Spin-cast layers of silicone bond the separate PZT MEHs.

Figure S17. *In vivo* evaluation of stacked PZT MEHs on voltage output. Voltage as a function of time for devices that incorporate (*A*) 3 and (*B*) 5 layers of PZT MEHs connected in series and mounted in the RV of a bovine heart (80 beats/min) at 0^{O} (left) and at 45^{O} (right).

Figure S18. The buckle amplitude of a single PZT MEH and that of each PZT MEH in the stacks, incorporating 3 and 5 PZT MEHs with spin-casted silicone layer of 10 μm thickness in between, for compression ΔL =5 mm. The differences between the amplitudes are very small, which suggests that the soft silicone layers do not make significant contribution to the deformation of the PZT MEHs.

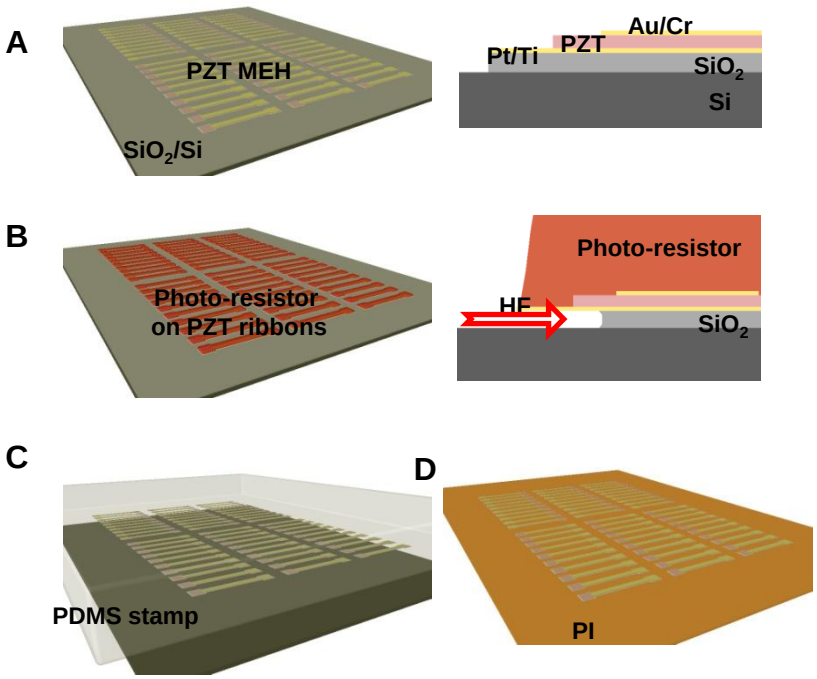
A
PZT MEH
SiO2/Si
Au/Cr
PZT
Pt/Ti
SiO2
Si
B
Photo-resistor
on PZT ribbons
Photo-resistor
HF
SiO2
C
PDMS stamp
D
PI

Figure S1

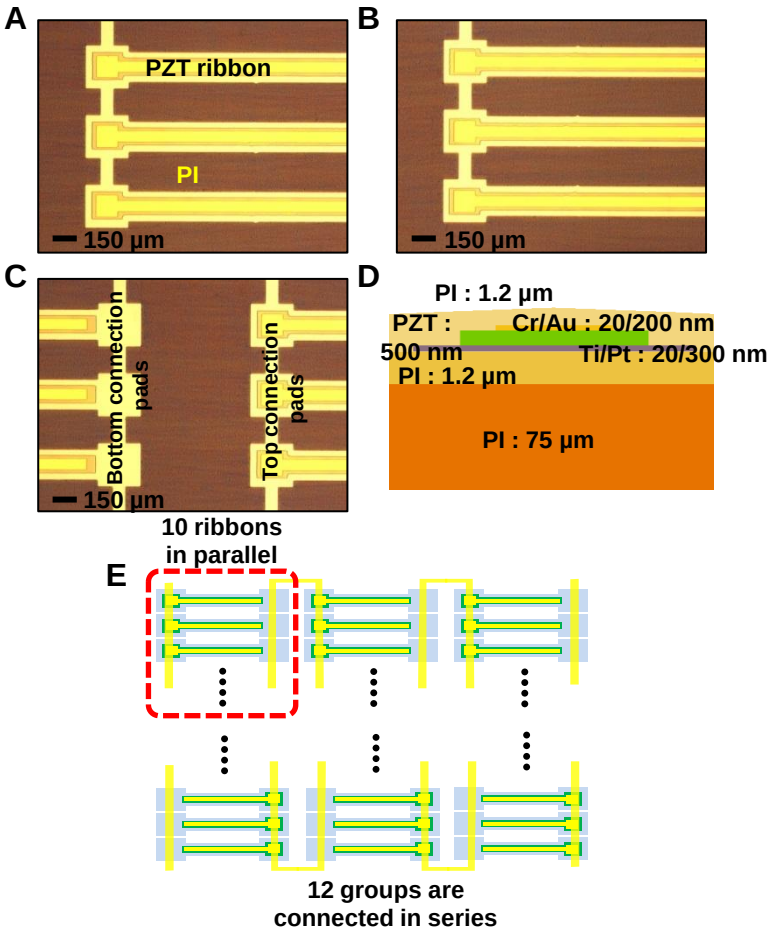
A
PZT ribbon
PI
150 μm
B
150 μm
C
Bottom connection pads
Top connection pads
150 μm
D
PI : 1.2 μm
PZT : 500 nm
Cr/Au : 20/200 nm
Ti/Pt : 20/300 nm
PI : 1.2 μm
PI : 75 μm
E
10 ribbons in parallel
12 groups are connected in series

Figure S2

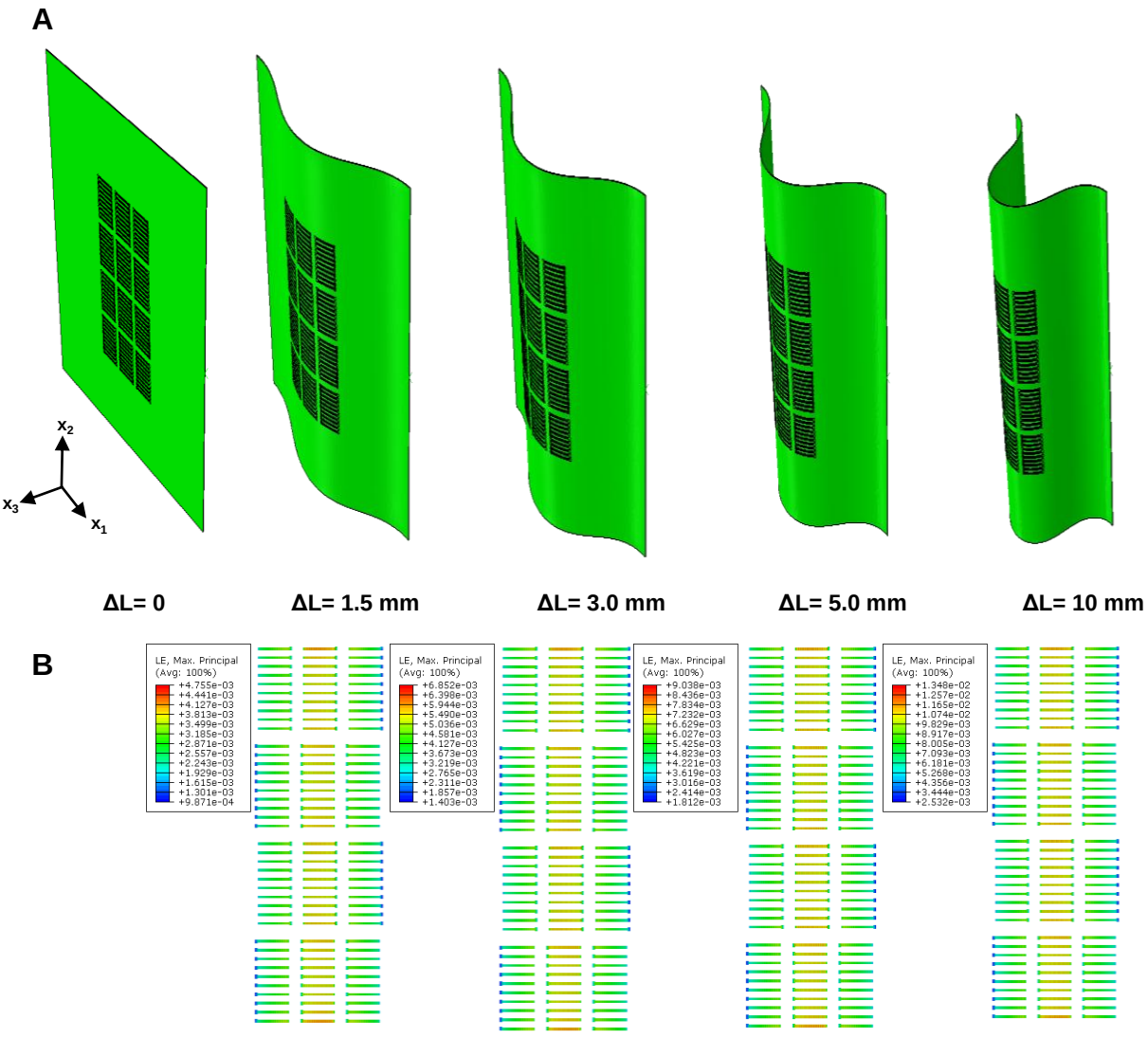
A
x2
x3
x1
ΔL= 0
ΔL= 1.5 mm
ΔL= 3.0 mm
ΔL= 5.0 mm
ΔL= 10 mm
B
LE, Max. Principal
(Avg: 100%)
+4.755e-03
+4.441e-03
+4.127e-03
+3.813e-03
+3.499e-03
+3.185e-03
+2.871e-03
+2.557e-03
+2.243e-03
+1.929e-03
+1.615e-03
+1.301e-03
+9.871e-04
LE, Max. Principal
(Avg: 100%)
+6.852e-03
+6.398e-03
+5.944e-03
+5.490e-03
+5.036e-03
+4.581e-03
+4.127e-03
+3.673e-03
+3.219e-03
+2.765e-03
+2.311e-03
+1.857e-03
+1.403e-03
LE, Max. Principal
(Avg: 100%)
+9.038e-03
+8.436e-03
+7.834e-03
+7.232e-03
+6.629e-03
+6.027e-03
+5.425e-03
+4.823e-03
+4.221e-03
+3.619e-03
+3.016e-03
+2.414e-03
+1.812e-03
LE, Max. Principal
(Avg: 100%)
+1.348e-02
+1.257e-02
+1.165e-02
+1.074e-02
+9.829e-03
+8.917e-03
+8.005e-03
+7.093e-03
+6.181e-03
+5.268e-03
+4.356e-03
+3.444e-03
+2.532e-03

Figure S3

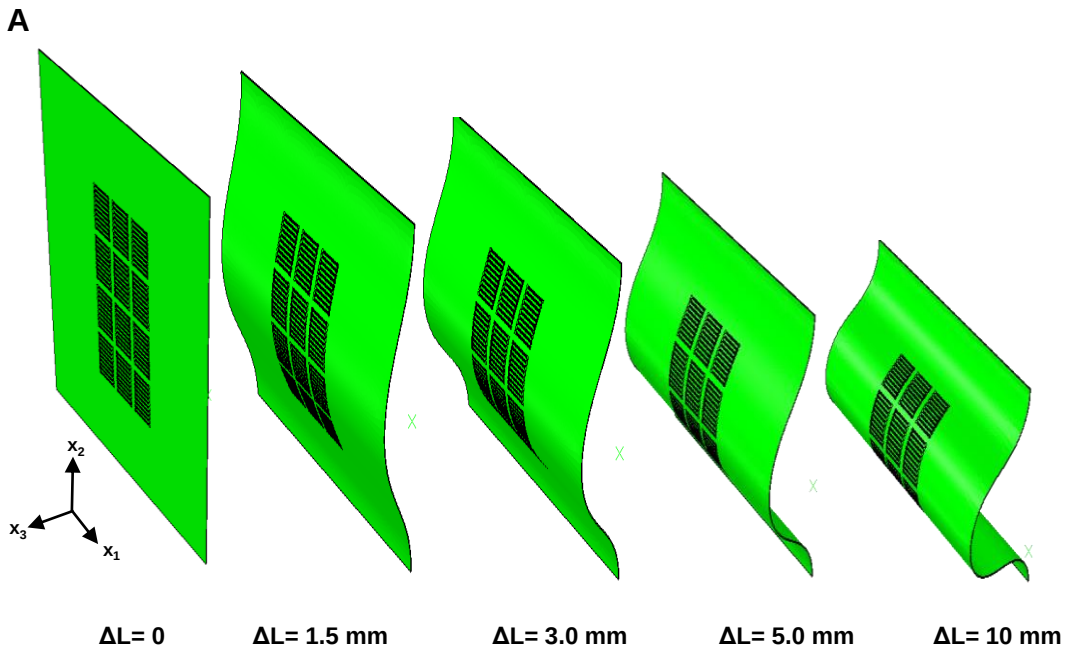
A
X2
X3
X1
ΔL= 0
ΔL= 1.5 mm
ΔL= 3.0 mm
ΔL= 5.0 mm
ΔL= 10 mm

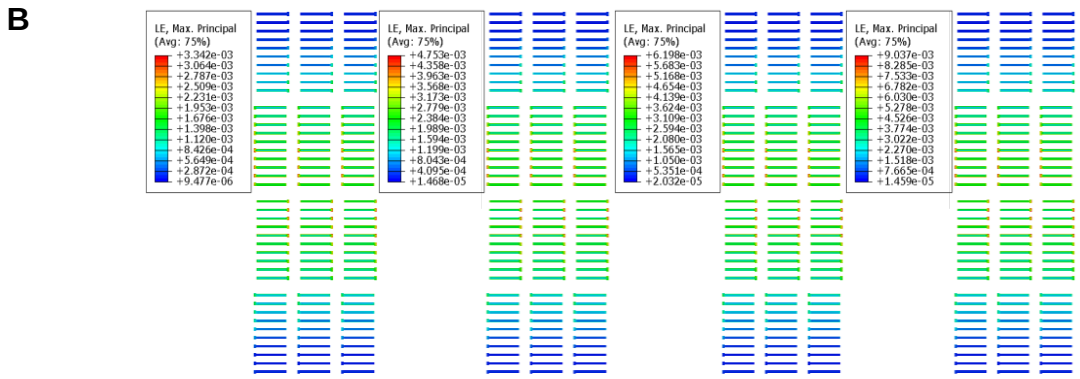
B
LE, Max. Principal
(Avg: 75%)
+3.342e-03
+3.064e-03
+2.787e-03
+2.509e-03
+2.231e-03
+1.953e-03
+1.676e-03
+1.398e-03
+1.120e-03
+8.426e-04
+5.649e-04
+2.872e-04
+9.477e-06
LE, Max. Principal
(Avg: 75%)
+4.753e-03
+4.358e-03
+3.963e-03
+3.568e-03
+3.173e-03
+2.779e-03
+2.384e-03
+1.989e-03
+1.594e-03
+1.199e-03
+8.043e-04
+4.095e-04
+1.468e-05
LE, Max. Principal
(Avg: 75%)
+6.198e-03
+5.683e-03
+5.168e-03
+4.654e-03
+4.139e-03
+3.624e-03
+3.109e-03
+2.594e-03
+2.080e-03
+1.565e-03
+1.050e-03
+5.351e-04
+2.032e-05
LE, Max. Principal
(Avg: 75%)
+9.037e-03
+8.285e-03
+7.533e-03
+6.782e-03
+6.030e-03
+5.278e-03
+4.526e-03
+3.774e-03
+3.022e-03
+2.270e-03
+1.518e-03
+7.665e-04
+1.459e-05

Figure S4

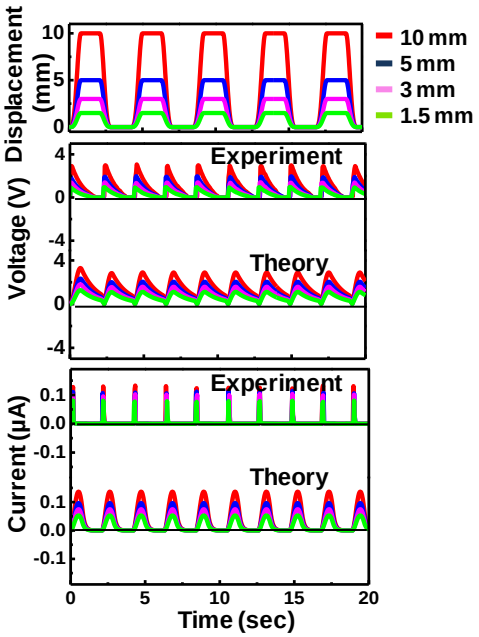
Displacement (mm)
10
5
0
10 mm
5 mm
3 mm
1.5 mm
Voltage (V)
Experiment
Theory
4
0
-4
Current (μA)
0.1
0.0
-0.1
0
5
10
15
20
Time (sec)

Figure S5

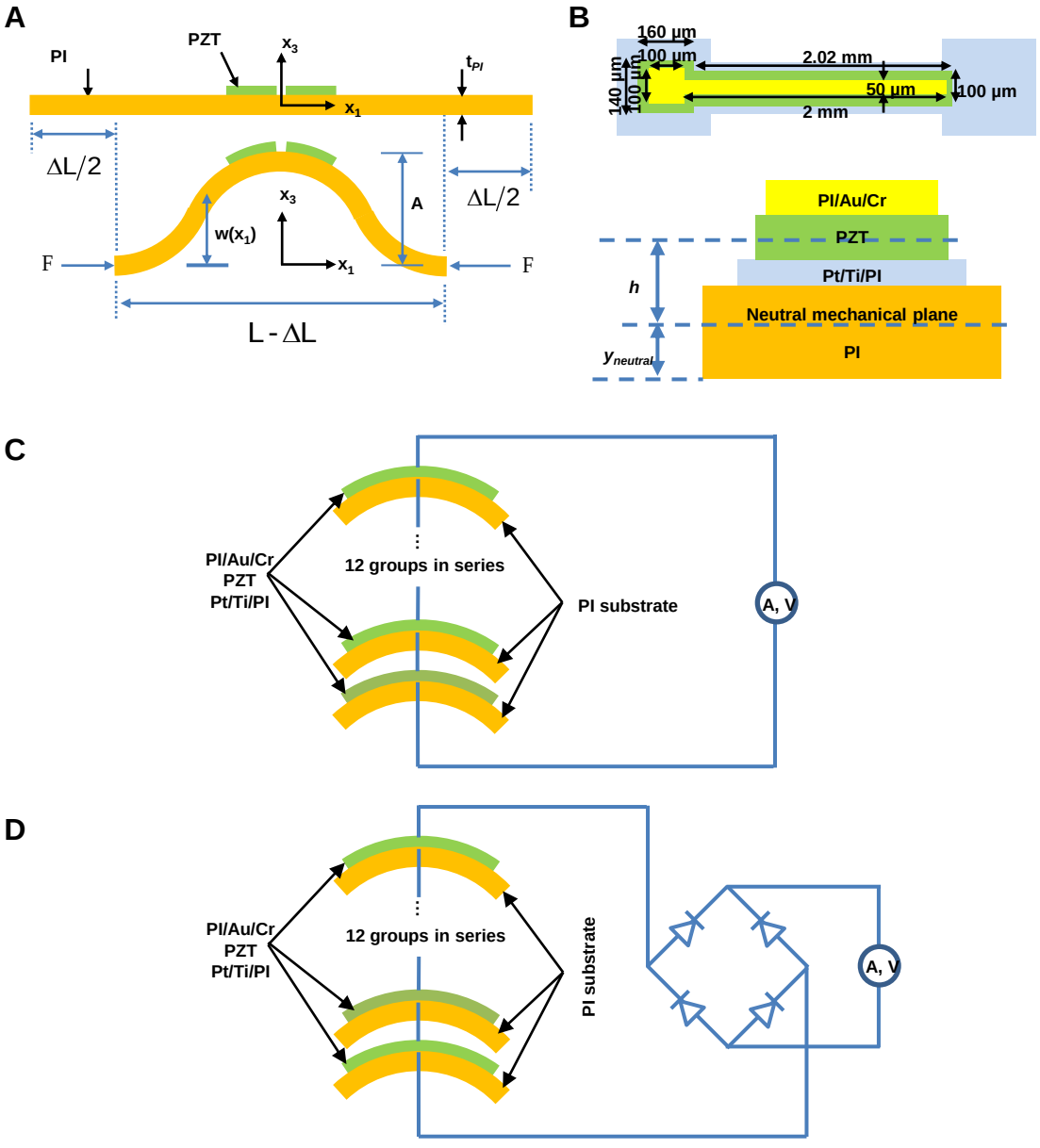
A
PI
PZT
x_3
t_{PI}
x_1
ΔL/2
ΔL/2
x_3
A
$w(x_1)$
F
x_1
F
L - ΔL
B
160 μm
100 μm
2.02 mm
140 μm
100 μm
50 μm
100 μm
2 mm
PI/Au/Cr
PZT
Pt/Ti/PI
Neutral mechanical plane
PI
h
$y_{neutral}$
C
PI/Au/Cr
PZT
Pt/Ti/PI
12 groups in series
PI substrate
A, V
D
PI/Au/Cr
PZT
Pt/Ti/PI
12 groups in series
PI substrate
A, V

Figure S6

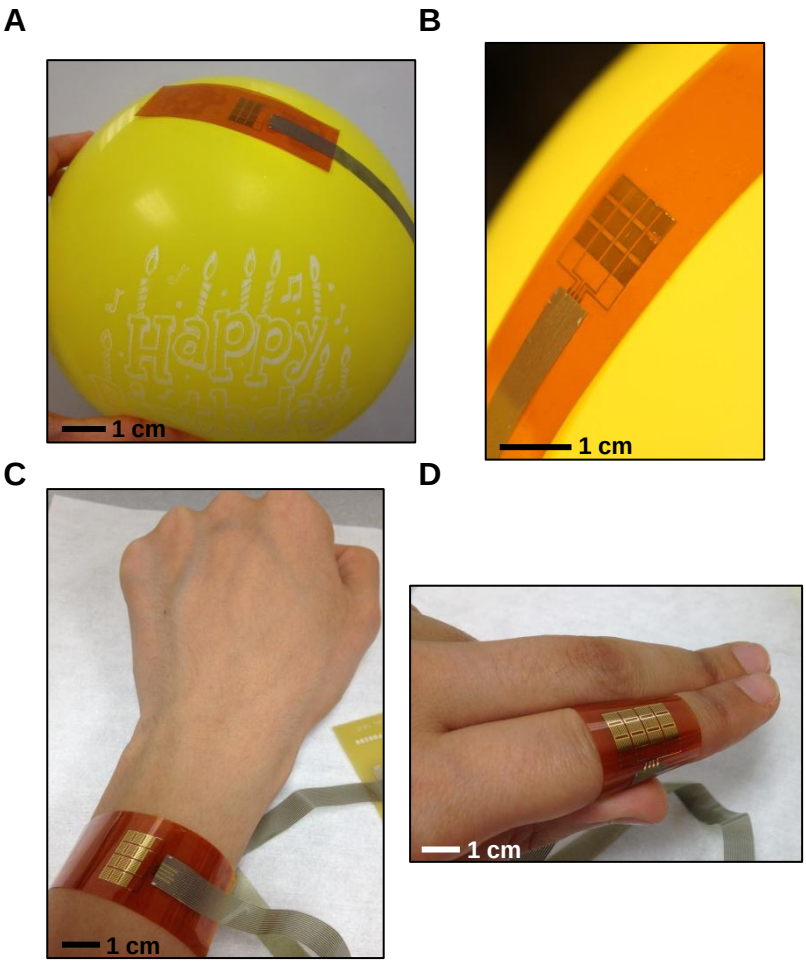

Figure S7

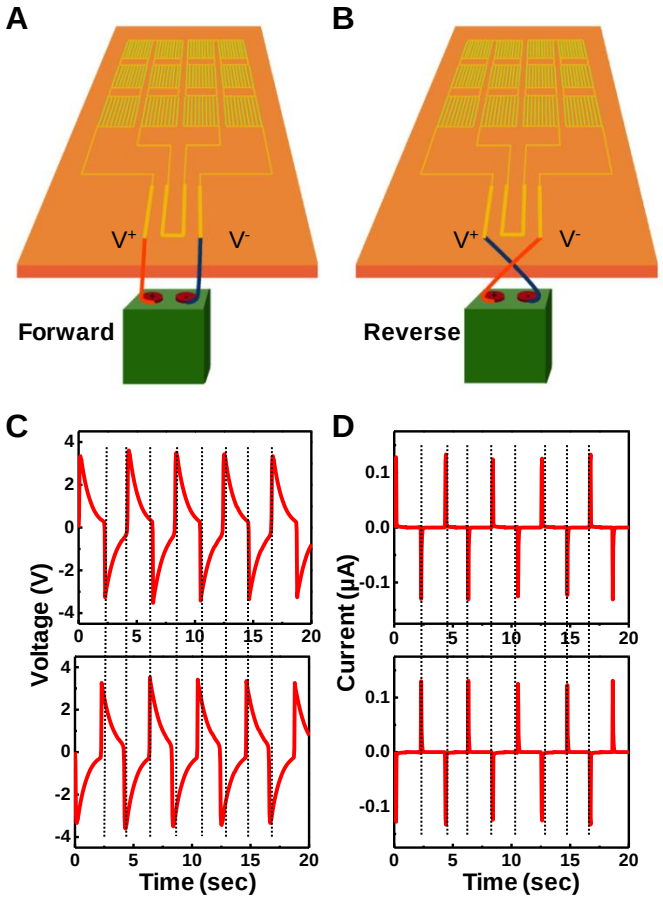
A
B
V+
V-
Forward
Reverse
C
D
Voltage (V)
Current (μA)
Time (sec)
Time (sec)

Figure S8

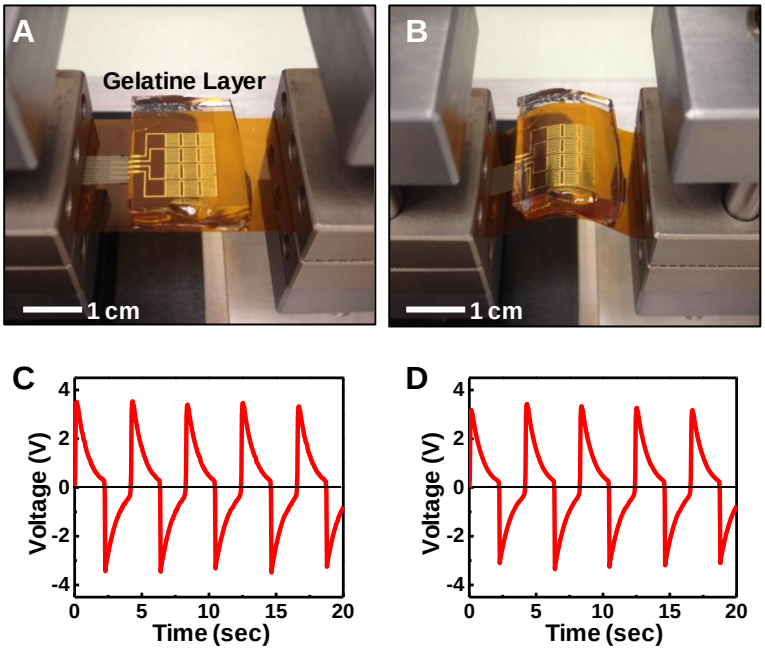
A
Gelatine Layer
1 cm
B
1 cm
C
Voltage (V)
Time (sec)
D
Voltage (V)
Time (sec)

Figure S9

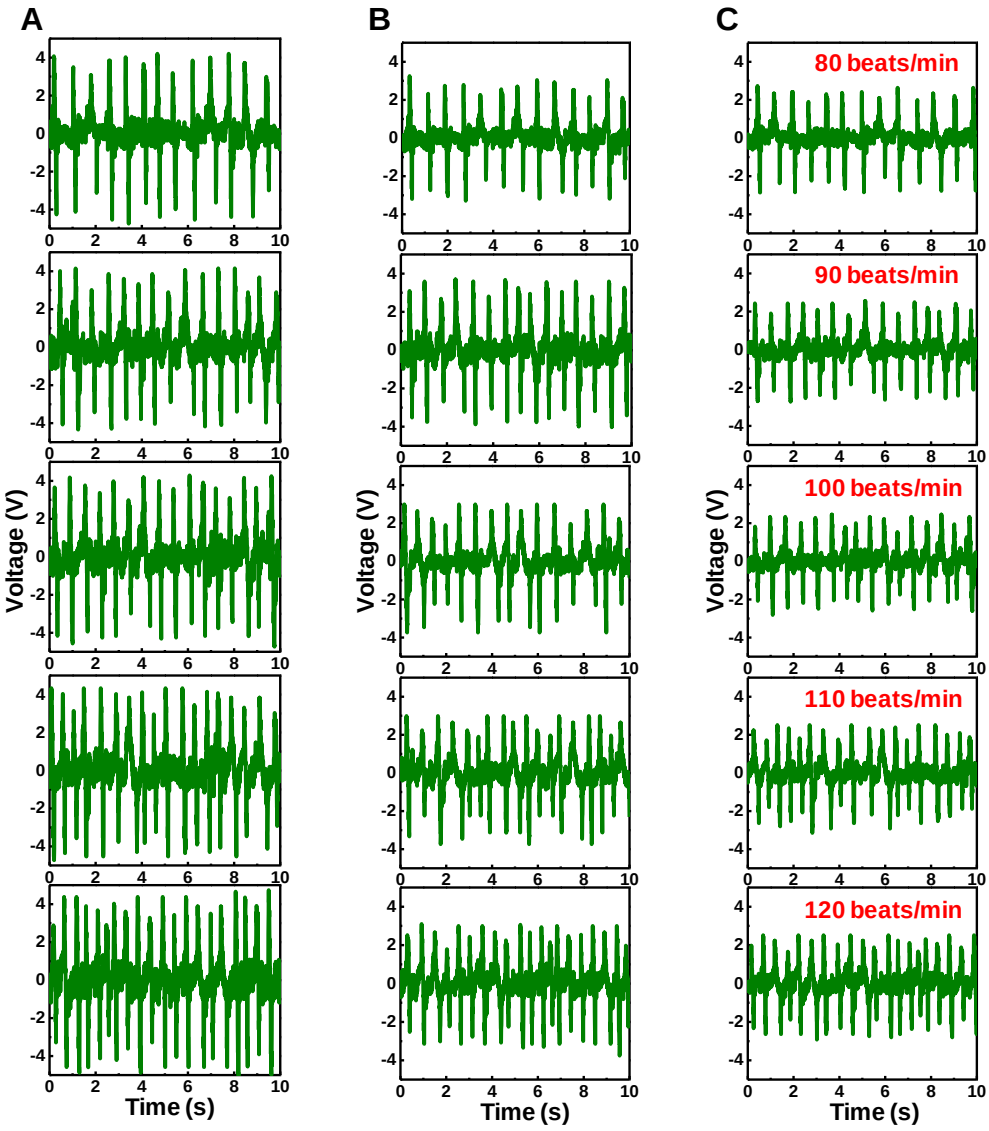
A
B
C
80 beats/min
90 beats/min
100 beats/min
110 beats/min
120 beats/min
Voltage (V)
Time (s)

Figure S10

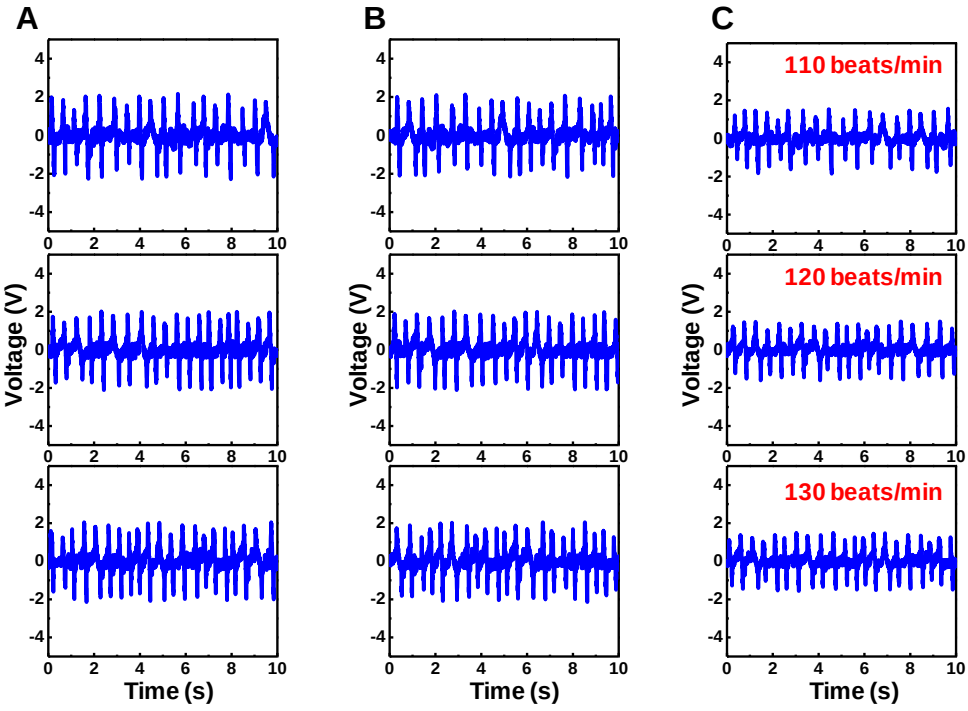

Figure S11

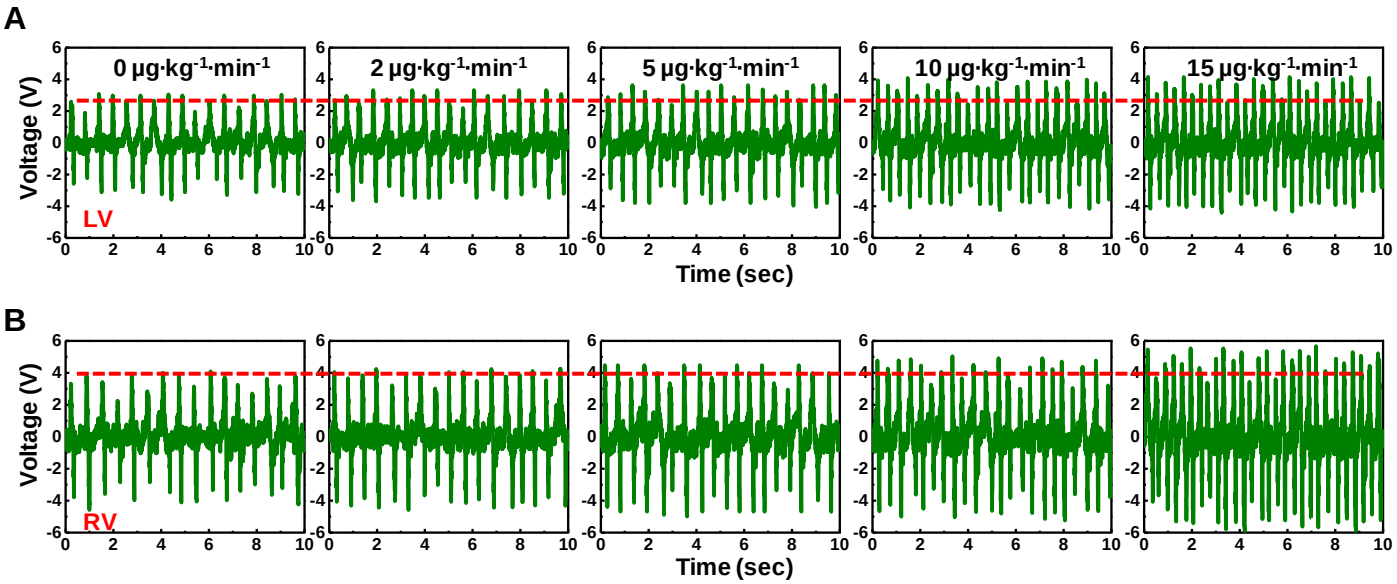
A
0 μg·kg-1·min-1
2 μg·kg-1·min-1
5 μg·kg-1·min-1
10 μg·kg-1·min-1
15 μg·kg-1·min-1
Voltage (V)
LV
Time (sec)
B
Voltage (V)
RV
Time (sec)

Figure S12

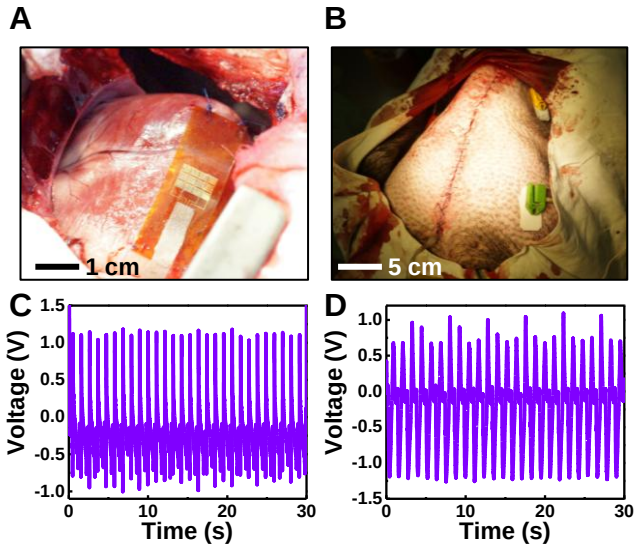

Figure S13

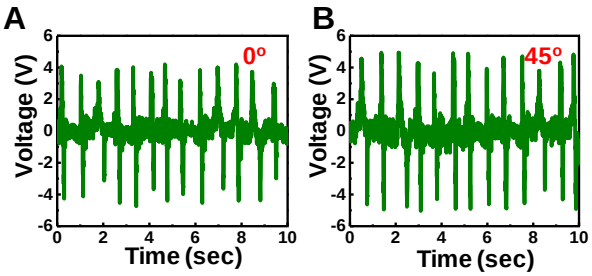

Figure S14

A

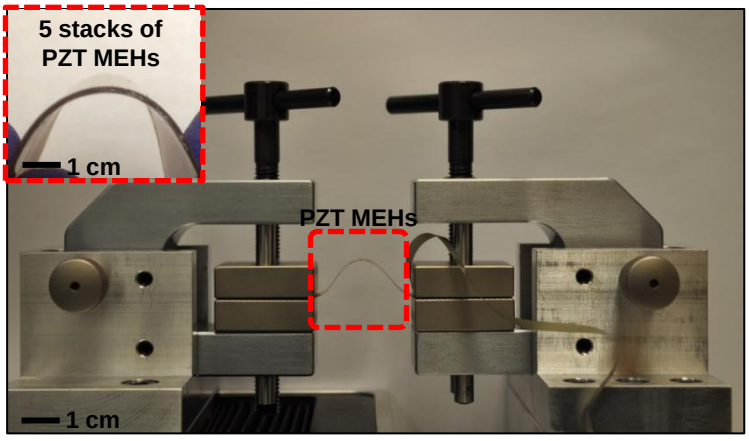

B

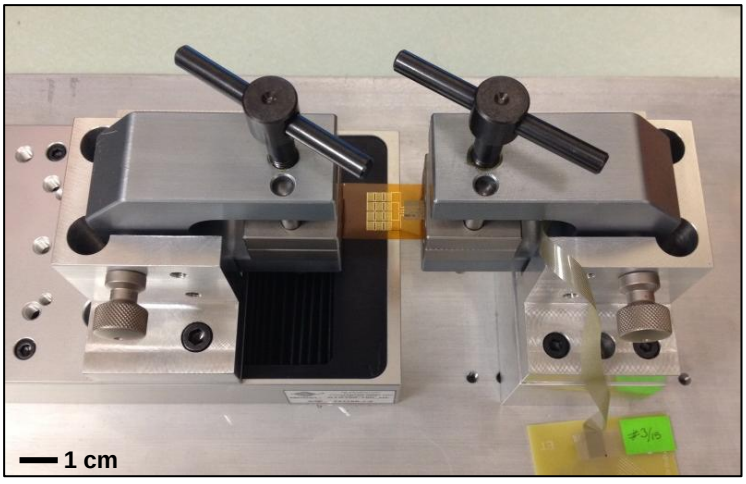

Figure S15

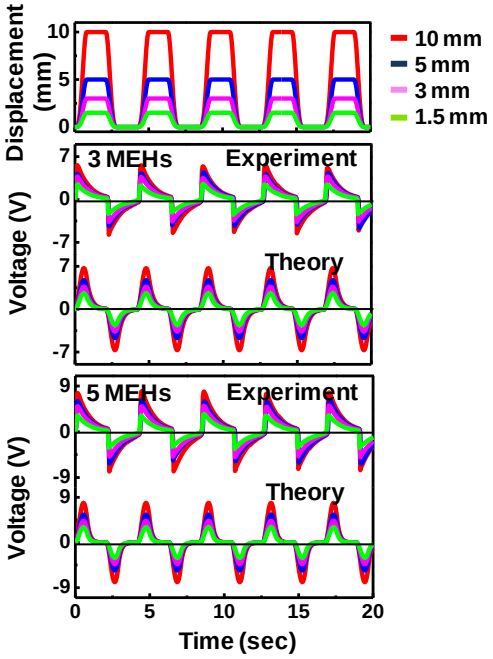
Displacement (mm)
10
5
0
10 mm
5 mm
3 mm
1.5 mm
3 MEHs
Experiment
Theory
Voltage (V)
7
0
-7
5 MEHs
Experiment
Theory
Voltage (V)
9
0
-9
0
5
10
15
20
Time (sec)

Figure S16

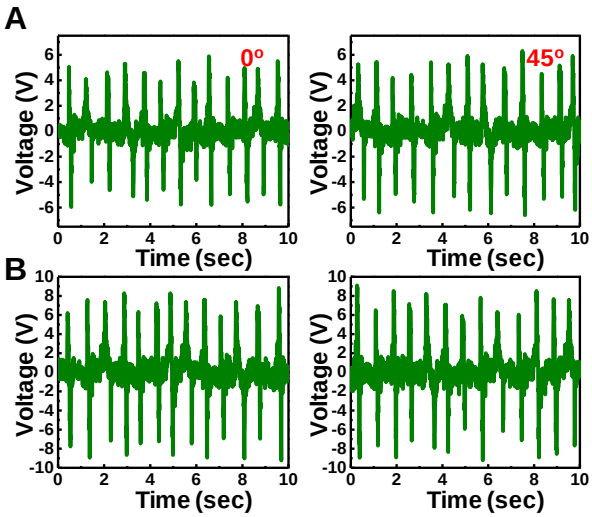

Figure S17

Table 1 The amplitude of the stacks for Δ*L*=5 mm.

	n^{th} PZT MEH	Amplitude (mm)
single PZT MEH	1	6.41
stack of 3 PZT MEHs	3	6.37
	2	6.37
	1	6.37
stack of 5 PZT MEHs	5	6.35
	4	6.35
	3	6.35
	2	6.35
	1	6.35

Figure S18